From gradual spreading to catastrophic collapse - Reconstruction of the 1888 Ritter Island volcanic sector collapse from high-resolution 3D seismic data

Jens Karstens[1], Christian Berndt[1], Morelia Urlaub[1], Sebastian F.L. Watt[2], Aaron Micallef[3], Melanie Ray[4], Ingo Klaucke[1], Sina Muff[1], Dirk Klaeschen[1], Michel Kühn[1], Theresa Roth[1], Christoph Böttner[1], Bettina Schramm[1], Judith Elger[1], Sascha Brune[5]

[1] GEOMAR Helmholtz Centre for Ocean Research Kiel, Germany

[2] School of Geography, Earth and Environmental Sciences, University of Birmingham, United Kingdom

[3] Marine Geology & Seafloor Surveying, Department of Geosciences, University of Malta

[4] Birkbeck, University of London, United Kingdom

[5]GFZ German Research Centre for Geosciences, Potsdam, Germany

*jkarstens@geomar.de

Abstract

Volcanic island flank collapses have the potential to trigger devastating tsunamis threatening coastal communities and infrastructure. The 1888 sector collapse of Ritter Island, Papua New Guinea (in the following called Ritter) is the most voluminous volcanic island flank collapse in historic times. The associated tsunami had run-up heights of more than 20 m on the neighboring islands and reached settlements 600 km away from its source. This event provides an opportunity to advance our understanding of volcanic landslide-tsunami hazards. Here, we present a detailed reconstruction of the 1888 Ritter sector collapse based on high-resolution 2D and 3D seismic and bathymetric data covering the failed volcanic edifice and the associated mass-movement deposits. The 3D seismic data reveal that the catastrophic collapse of Ritter occurred in two phases: (1) Ritter was first affected by deep-seated, gradual spreading over a long time period, which is manifest in pronounced compressional deformation within the volcanic edifice and the adjacent seafloor sediments. A scoria cone at the foot of Ritter acted as

a buttress, influencing the displacement and deformation of the western flank of the volcano and causing shearing within the volcanic edifice. (2) During the final, catastrophic phase of the collapse, about 2.4 km³ of Ritter disintegrated almost entirely and travelled as a highly energetic mass flow, which incised the underlying sediment. The irregular topography west of Ritter is a product of both compressional deformation and erosion. A crater-like depression underlying the recent volcanic cone and eyewitness accounts suggest that an explosion may have accompanied the catastrophic collapse. Our findings demonstrate that volcanic sector collapses may transform from slow gravitational deformation to catastrophic collapse. Understanding the processes involved in such a transformation is crucial for assessing the hazard potential of other volcanoes with slowly deforming flanks such as Mt. Etna or Kilauea.

Keywords: Volcanic sector collapse, Ritter Island, landslide, tsunami, 3D seismic interpretation

Highlights:

- First 3D seismic cube covering a failed volcanic flank and its slide deposits
- Slow gradual spreading may transform into catastrophic collapse
- Hummocky deposit topography is an interplay between compressional deformation and erosion
- Only ~15% of total slide volume contributed to tsunami genesis

1. Introduction

The remnants of volcanic sector collapses have been identified around volcanic islands worldwide and are among the largest known mass flow events on Earth, with volumes of up to 5000 km^3 in case of the Nuuanu landslide offshore Hawaii (Moore et al., 1989). Computer simulations indicate that large-scale volcanic landslides on oceanic islands such as Hawaii or the Canaries can cause ocean-wide tsunamis (Løvholt et al., 2008; Waythomas et al., 2009). However, the magnitude of these tsunamis is poorly constrained, since tsunami generation depends on complex landslide transport and emplacement processes (Harbitz et al. 2013). Proximal tsunami run-up heights of more than 100 m on

54 neighboring coastlines have been identified for flank-collapse generated tsunamis in Hawaii, Cape
55 Verde, and the Canary Islands (McMurtry et al., 2004; Ramalho et al., 2015; Paris et al., 2017).
56 Recent studies have shown that emplacement processes are often more complicated than previously
57 assumed, involving seafloor sediment incorporation and eruptive activity (Watt et al. 2012, Hunt et al.
58 2013). A robust understanding of these factors is essential for assessing the hazard of volcanic sector
59 collapses.

60 In historic times, volcanic landslide-induced tsunamis have caused more than 15,000 casualties, most
61 of which can be attributed to the collapse events of Oshima-Oshima, Japan, in 1741, Mt. Unzen,
62 Japan, in 1792, and Ritter, Papua New Guinea, in 1888 (Siebert et al., 1987; Auker et al., 2013; Day
63 2015). All of these events occurred at composite arc volcanoes. Flank collapses in arc settings are
64 typically smaller than those at ocean islands, but have a much higher global frequency and provide all
65 historical examples (Watt et al., 2014; Day et al., 2015). Despite differences in the mobilized
66 volumes, the deposits of sector collapses around ocean islands and island arc volcanoes are similar in
67 various aspects, such as slope gradients in the deposition area, relationship between volume and loss
68 of relief/run-out, nature of blocks and matrix of the deposit, as well as the geometry and size of blocks
69 with respect to the collapsed volume (McGuire 2006; Watt et al., 2014). This suggests that the
70 controlling processes and mechanisms are broadly similar, and insights from studying Ritter allow an
71 improved understanding of volcanic sector collapse processes and associated tsunami generation in
72 general.

73 The 1888 Ritter sector collapse is the largest historic volcanic island sector collapse (Day 2015).
74 Contemporary reports provide detailed information on the resultant landslide-induced tsunami
75 (Anonymous, 1888; Steinhäuser, 1892). On the early morning of March 13, a large fraction of the
76 island slid into the Bismarck Sea and triggered a devastating tsunami (Day and Ward, 2003).
77 Observations suggest a single wave train, and hence a single phase of tsunami generation. The
78 tsunami had a run-up height of more than 20 m on the neighboring islands and was still observed
79 more than 600 km away from Ritter (Ward and Day, 2003; Day et al., 2015). Eyewitness accounts
80 from various settlements allow a detailed reconstruction of the tsunami propagation, even though

there are no direct observations of the collapse itself. Previous geophysical investigations showed that the emplacement of the Ritter debris avalanche was guided by the complex local seafloor morphology, with channelization between the neighboring islands of Umboi and Sakar, and an influence of submarine volcanic ridges and cones on the dispersal of the deposit (Day et al., 2015; **Fig. 1**). The volcanic ridges divide the deposit into two regions: (i) a proximal region with an irregular surface, previously interpreted as a blocky debris avalanche facies similar to the deposits produced by the 1980 Mount St. Helens sector collapse, and (ii) a distal deposit interpreted as comprising finer-grained debris flow and turbidite deposits, including the failure and incorporation of pre-existing seafloor sediment (Day et al., 2015). Based on hydroacoustic data and cone reconstructions, it was previously estimated that the Ritter debris avalanche mobilized about 4.2 km³ of the volcanic edifice, and that the distal deposits have a volume of 6.4 km³ with a high proportion of eroded seafloor sediments (Day et al., 2015).

In late 2016, we acquired a comprehensive dataset including a high-resolution three-dimensional (3D) seismic P-Cable cube covering the proximal part of the 1888 mass-movement deposits, more than 1000 km of two-dimensional (2D) reflection seismic profiles, high-resolution bathymetry, rock samples, as well as seafloor video imagery. The 3D seismic data provide the first-ever insights into the subsurface of the source region of a volcanic landslide. The first and main objective of this study is to reconstruct the 1888 Ritter sector collapse and to constrain the emplacement dynamics of the resulting mass-movement. We combine 2D and 3D seismic data with morphological observations and seafloor imagery to understand the dynamic slide development and to establish a chronological framework for the destabilization and mobilization of the western flank of Ritter. Our second objective is to reconstruct the preconditions that led to destabilization of Ritter's western flank and the processes that triggered the catastrophic collapse in 1888. Our third objective is to evaluate the implications for the interpretation of volcanic landslide deposits in a submarine environment and for tsunami hazard assessment.

2. Geological background

2.1. The Bismarck volcanic arc and Ritter

Ritter is located in the center of the Bismarck arc, which is part of a tectonically complex zone of microplates between the Pacific and Australian plates (**Fig. 1A**; Woodhead et al., 2010; Baldwin et al., 2012). It marks the transition from typical arc magmatism in the east, to magmatism associated with subduction of the remnant Solomon Sea slab and arc-continent collision in the west (Johnson 1977; Woodhead et al., 2010; Holm and Richards, 2013). Analyses of rock samples show that basaltic melts dominate the volcanism of the Western Bismarck arc (Johnson, 1977; Woodhead et al., 2010), which includes Ritter. Seafloor mapping revealed debris avalanche deposits around eleven volcanoes, showing that sector collapses are a widespread geological phenomenon in the Bismarck arc (Silver et al., 2009).

Ritter is a relatively small and morphologically young conical edifice, rising from a base at ~1000 m beneath sea level, with a basal diameter of ~7 km. It lies between the larger islands of Umboi, New Britain and Sakar (**Fig. 1B**). Visual observations at Ritter, along with both subaerial and submarine samples, suggest that small-scale basaltic explosive and effusive volcanism characterized the volcano throughout its history, which is consistent with its simple conical shape and historical descriptions (Johnson, 2013; Day et al., 2015). More recent observations confirm that the volcano has continued to be active following the 1888 collapse (**Fig. 2;** Saunders and Kuduon, 2009). A horse-shoe-shaped slide scarp formed by the 1888 sector collapse dominates the morphology of Ritter. Lying centrally at the foot of the collapse scar, a prominent mound has been interpreted as an intact flank segment (i.e. toreva block, **Fig. 2,** Day et al., 2015). A new volcanic cone with a well-developed summit crater (approximately 200 m below sea-level at present) has grown after 1888 in the center of the slide scarp (Day et al., 2015). According to subaerial observations (Saunders and Kuduon, 2009), the volcanic cone has been active in recent times. Several conical scoria cones west of Ritter were previously interpreted to have formed after 1888 (Day et al. 2015).

2.2. Historic eyewitness accounts of the 1888 events

Ritter was described as a prominent landmark by explorers sailing the Bismarck Sea since the late 17th century (Johnson, 2015), with observers noting frequent eruptive activity (interpreted as Strombolian explosive eruptions). Two eruptions in the southern Bismarck Sea, with unconfirmed dates of 1878 and 1887, may have been at Ritter (Johnson, 2015), suggesting that the island was likely volcanically active shortly before it collapsed. Prior to collapse, Ritter was described as a steep-sided, ~800 m high cone. There are no historic accounts about volcanic activity, earthquakes or other precursors immediately before or during the 1888 sector collapse, but the resulting tsunami was described by German colonists at various settlements along the coasts of New Guinea and New Britain (Anonymous, 1888; Steinhäuser, 1892). Previous investigations concluded that the Ritter collapse was most likely not preceded, accompanied, or followed by magmatic eruption, and it was thus classified as a Bandai type collapse (Day et al., 2015). However, there are eyewitness accounts that suggest explosions may have accompanied the 1888 collapse. These accounts recall a shot-like noise (which could plausibly originate from a phreatic explosion, given that comparable sounds are described accompanying the Bandai sector collapse; Sekiya and Kikuchi, 1890) about 40 minutes before the arrival of the tsunami wave in Hatzfeldthaven, 350 km to the west, and a thunder-like sound and ash fall in Finschhafen, 100 km to the south. The latter observation is hard to explain, given the lack of evidence of more proximal tephra fall deposits or a high eruption column, but additional reports of washed-up pumice at the north coast of New Guinea, as well as ash and pumice clasts reported on top of tsunami-devastated rain forest along the west coast of New Britain, 20 km east of Ritter, in the days after the collapse (Anonymous, 1888; Steinhäuser, 1892), do suggest possible magmatic activity accompanying the event. Although alternative explanations may be made to account for some eyewitness descriptions, comparisons with Bandai suggest that a phreatic explosion was likely to have accompanied the event, particularly given that the collapse scar cross-cuts the recently active conduit and would have led to seawater interaction with the shallow plumbing system. The interpretation of accounts that suggest subaerial magmatic activity accompanying the event remain more ambiguous.

3. Data and methods

During cruise SO252 with R/V Sonne in late 2016 we collected a 3D seismic survey using a P-Cable 3D seismic system consisting of sixteen streamers and two 105/105 cubic inch GI airguns in harmonic mode. The survey covered about 60 km² (**Fig. 1c**). Data processing included source-receiver geometry corrections, bandpass frequency filtering, normal move-out correction, stacking, trace-interpolation, and 3D time migration using a constant velocity of 1500 m/s. The resulting 3D cube has a lateral resolution of 3.25 m and vertical resolution of approximately 6 m at the seafloor (decreasing with depth). The 2D seismic profiles were recorded using the same airgun source and a 250 m-long streamer (160 channels) with a group spacing of 1.56 m. 2D seismic data processing included bandpass filtering, normal move-out correction, and 2D stolt-migration using a constant velocity of 1,500 m/s. In addition, we acquired a bathymetric grid of the study area with a horizontal resolution of 5 m using two multibeam systems (Kongsberg EM710 and EM122). Six three-component ocean bottom seismometers (OBS) were deployed along a profile within the 3D seismic cube to derive a 2D velocity model by forward modeling. The OBS data analyses included interactive phase picking, velocity model editing, and comparison of measured and modeled arrivals using the software tools PASTEUP and MODELING (Fujie et al., 2008). Combination of 3D seismic interpretation with seismic velocity information from the OBS experiment allows us to derive depth and volume information. We integrated and analyzed the datasets using the seismic interpretation software package Petrel by Schlumberger and KingdomSuite by IHS. In addition, we collected seafloor video and photographic footage as well as rock and sediment samples during ten dives using the remotely operated Ocean Floor Observation System, a TV grab and a Hydraulic Benthic Interactive Sampler System.

4. Results

4.1. The morphology of Ritter and the adjacent seafloor

The submarine morphology of Ritter is dominated by the horseshoe-shaped scarp of the 1888 sector collapse, which consists of northern and southern submerged sidewalls, extending westwards from the crescent shaped remnants of the subaerial part of the island (**Fig. 2A**). The current island was part of

188 the eastern flank of the cone, and the collapse cut through the central conduit, leaving the position of
189 the former island summit submerged. A submarine cone lies within the collapse scar, and from its
190 position and seismic character we infer that this cone has been built by continued post-1888 eruptions
191 from the pre-collapse conduit system. The summit of this cone has a crater filled with turbid water
192 indicating vigorous ongoing hydrothermal activity.

193 The morphology of the slide scarp is generally smooth, although seafloor video footage reveals the
194 walls to be incised and irregular, comprising exposed, brecciated lavas interbedded with primary and
195 reworked scoriaceous deposits, which are extensively cut by volcanic dykes (**Figs. 2A-D**). A chain of
196 small parasitic cones on the intact southern flank of Ritter is radially aligned with the crater of the
197 post-1888 cone (**Figs. 2A, 3**).

198 Large, submarine conical features mark the basin west of Ritter, in some cases forming ridges aligned
199 NNE between Umboi and Sakar. Seafloor imagery indicates that the surface of these cones consists of
200 well-bedded, scoriaceous deposits. Therefore, we interpret them as either isolated or aligned clusters
201 of monogenetic scoria cones, although most have no summit crater. Except for these volcanic cones
202 and ridges, the slopes of Umboi and Sakar have a generally smooth morphology with several gullies
203 (**Fig. 1C**). The morphology becomes slightly rougher at the base of the Umboi slope; the transition
204 between smooth and rougher morphology has been interpreted as a trim line related to the 1888
205 landslide (Day et al., 2015).

206 The seafloor morphology west of Ritter's new cone is relatively flat and smooth, although it is marked
207 by gently undulating parallel ridges. These features occur across the northern half of the basin, from
208 the Ritter slide scarp to the volcanic ridges in the west, and align broadly N-S and thus
209 perpendicularly to the inferred direction of landslide movement (**Fig. 2G**). In contrast, the southern
210 half of the basin is characterized by much more irregular topography, comprising steep-sided mounds
211 with no regular alignment or fabric, which are separated by a network of channels (**Fig. 2B, H**). Based
212 on analogy with subaerial debris avalanche deposits, this terrain may be described as hummocky.
213 Individual hummocks are very large, with widths of a hundred to more than a thousand meters. The
214 boundary between the relatively flat, gently ridged terrain and the hummocky terrain to the south

marks a topographic step (**Fig. 2B, G**), with the summits of the hummocks being all topographically lower than the level of the flat terrain further north. Seafloor video footage and sampling from the steep sides of the hummocks indicates sand- to cobble-sized loose volcanoclastic sediment at the surface (**Fig. 2E**). The network of channels between the hummocks deepens towards the west. For example, two channels originate north and south of the scoria cone west of the toreva block and become successively deeper towards the west (**Figs. 2B, H**), while another channel originates between the volcanic ridges at the northwestern corner of the basin (**Fig. 2H**). All channels merge into one major, >50 m deep channel that continues into the neighboring basin west of the ridges (**Figs. 1C, 2**).

4.2. Internal architecture of Ritter and the adjacent seafloor

The seismic data reveal that Ritter consists of well-stratified material (**Fig. 3**). Undisturbed, sub-parallel layers characterize the northern flank of Ritter, while the southern flank shows pronounced deformation and a more complex internal architecture. Reflections with higher amplitudes may mark the division between different phases of pre-collapse growth of the volcano. The southern flank of Ritter has grown on top of the northward dipping strata of the slope of Umboi. The seismic data clearly show a chain of parasitic cones that have grown during the deposition of the youngest unit of pre-collapse deposits, indicating that these features are comparatively young (**Figs. 3**). An unconformity marks the boundary between the post-1888 cone and the older volcanic edifice, indicating that the new cone has filled up a crater-like depression (**Fig. 3**).

Seismic profiles crossing the volcanic cones and ridges on the slope and west of Ritter support our interpretation that these features are scoria cones, revealing an internal structure of continuous, low-amplitude, surface-parallel reflections. (**Figs. 2F, 4**). The toreva block, which lies between two chutes on either side of Ritter's collapse scarp, has a well-preserved internal stratification that resembles that of Ritter (**Figs. 2A, 4D**). Strongly folded reflections at the western foot of the toreva block indicate shortening and overlie the neighboring scoria cone. At the base of these folded reflections, a thrust fault is visible in the seismic data and manifests as a subtle ridge on the seafloor that extends North and South of the Toreva block margins (**Figs. 6, 7**).

242 At the foot of the collapse scar, extensive compressional deformation structures extend into well-
243 stratified units for more than 500 m below the present-day seafloor. This deformation is most intense
244 beneath the chutes to the north and south of the toreva block, and is less pronounced in the toreva
245 block itself (**Figs. 4, 5**). In the region extending west from the southern chute of the collapse scarp,
246 several angular units with well-preserved but inclined strata indicate rotation of intact blocks with
247 diameters of 500 – 1000 m (**Fig. 5**). The rotational deformation close to Ritter gradually turns into
248 symmetrical folding towards the west, extending over 8 km from the collapse scarp and affecting
249 sedimentary units with a well-preserved internal stratification. The folded package has a thickness of
250 up to 150 m. Towards the west, the fold crests have been partly eroded, truncating internal
251 stratigraphy. The folded sediment package that extends from the northern segment of the collapse
252 scarp is less affected by erosion and the folds have shorter wavelengths (**Fig. 4**). Two high-amplitude
253 reflections mark boundaries between sediment packages affected by different degrees of deformation
254 (**Figs. 4, 5**). Although these distinct reflections are discontinuous, it is possible to map the lower of
255 these two shear zones, which marks the base of extensive deformation, across the entire basin. The
256 seismic dataset is not depth converted and, thus, some of the bending of the reflections may be
257 attributed to velocity pull-ups. However, most of the bending reflects folding, which becomes clear,
258 when flattening the seafloor reflection and is also demonstrated by the wide-spread presence of
259 bending beneath areas with flat seafloor. Immediately south of Ritter, the base of deformation
260 converges with the unconformity between the slope of Umboi and the base of the Ritter edifice (**Figs.**
261 **3-5**). The intense folding and faulting in the upper basin stratigraphy persists across both the
262 hummocky terrain and the flatter, ridged terrain to the north. The crests of the ridges in the northern
263 half of the basin appear to coincide with fold axes, while some crests in the hummocky terrain in the
264 south also appear to reflect anticlinal folds or faulted blocks within the bedded sediment package
265 (**Figs. 4, 5**).

266

267 ### 4.3. Volume estimates and quantification of shortening

The OBS data yield seismic velocities of ~1760 m/s for the deformed basin infill (Roth, 2018). Mapping the lower shear zone as the base of material deformed by the 1888 collapse in 2D and 3D seismic data (yellow in **Fig. 3- 5**) and converting it to depth by extrapolating the OBS velocities laterally results in a volume of 11 +/- 1 km³ (**Fig. 8B**). Although the error of the velocity field is of the order of 100 m/s at this depth interval, the total uncertainty is about 10% because the data do not provide information on the lateral variability of the P-wave velocity. This volume includes the toreva block and extends into the chutes of the collapse scar, but excludes scoria cones in the basin. The volume missing from Ritter (i.e. the portion of the pre-collapse cone that was entirely evacuated from the collapse scarp) was reconstructed by fitting ellipsoids to the contour lines of the present day bathymetry and assuming a pre-collapse summit height of 800 m (projected from remaining flanks and consistent with pre-collapse descriptions; cf. Day et al., 2015), which resulted in a volume of 2.4 +/- 0.2 km³ (**Fig. 8A**). The volume of sediments eroded by the channel network on the south side of the basin was approximated by interpolating between the margins of the erosional channel systems within the 3D seismic data, to a height consistent with the projected surface of the flat region on the north side of the basin. This results in a volume of 1.6 +/- 0.1 km³ of eroded material from these channels (**Fig. 8C**).

Quantifying the amount of shortening is difficult because of the imperfect imaging of compressional structures within the deformed seafloor sediments. Geometric analysis of individual structures suggests compression of 12 to 24 m per kilometer, but it is clear that this is only a minor part of the shortening. A more useful estimate of the total shortening may be the observed movement of the toreva block, which has moved about 600 m into the deformed sediments. This total maximum shortening corresponds to 60 m/km, which agrees reasonably well with the shortening derived from individual structures considering that most deformation occurs at sub-seismic scales (e.g. Barnes et al., 2018)..

5. Discussion

The seafloor morphology and the internal architecture of the remnants of Ritter and the adjacent bedded sedimentary units indicate a complex development of the 1888 sector collapse. The exposed

and evacuated slide scarp clearly indicates an unconfined catastrophic failure of the volcanic cone during the 1888 event. The basal surface of this evacuated scarp continues from the failed edifice to overlie compressively deformed bedded sediments west of Ritter. This suggests that a first phase of flank instability must have preceded the disintegrative phase (**Figs. 4-6**). In the following we discuss each collapse phase and their implications.

5.1. Deep-seated spreading of the western flank of Ritter

A key for the reconstruction of the deep-seated deformation at Ritter is the toreva block, which represents an intact remnant of the failed western flank and therefore preserves the deformation history of the volcano before the catastrophic collapse. The toreva block reveals well-preserved internal stratification characterized by pronounced folding at its western toe. The amplitude of folding increases with depth, indicating that compressional deformation (i.e. westward spreading at the base of the flank) accompanied growth of the volcanic edifice (**Fig. 7A**). The current position of the toreva block relative to contours of the remaining edifice indicates that the block was laterally displaced by at least 1 km (**Fig. 7B**). It is likely that part of this displacement may reflect translation on a slide surface during the catastrophic phase of collapse, but there is evidence that there was also a long-term movement associated with spreading at the base of the flank. The folded sediments within the toreva block abut the flanks of a partly buried scoria cone, which pre-dates the 1888 collapse (**Fig. 4C**). The scoria cone may thus have acted as a buttress for the central segment of the spreading, western flank of Ritter, which explains the preservation and limited displacement of the toreva block relative to material evacuated along the chutes to the north and south. This situation may be, although on a far smaller scale, comparable to the unstable southern flank of Kilauea, where the cone of Loihi controls the development of the Hilina Pali slump (Smith et al., 1999). Deep-seated gradual spreading within volcanic edifices is a well-documented process and currently active flank movements are observed at several volcanoes (e.g. Kilauea, and Etna; Morgan et al, 2003; Urlaub et al., 2018). Gradual spreading can induce structural instability of the volcanic edifice, which may ultimately lead to the catastrophic collapse of the volcano along deep-seated detachments with the incorporation of large amounts of

basement material (van Wyk de Vries & Francis, 1997). The observed folding and thrusting at Ritter is similar to field geological observations from onshore volcanoes affected by deep-seated gradual spreading like Socompa (Chile; van Wyk de Vries et al. 2001), Mombacho (Nicaragua; van Wyk de Vries & Francis, 1997) or Jocotitlan (Mexico; Dufresne et al., 2010).

The bedded packages north and south of the toreva block have experienced far stronger deformation and are characterized by a complex interplay of compressional folding, thrust faulting and rotation of blocks reaching down to 500 meters deep (**Figs. 4-6**). The timing and duration of spreading at the base of the Ritter edifice, and how this relates to the compressional deformation that extends through much of the basin sediment west of Ritter, is difficult to constrain. However, the increase in fold amplitude with depth in the toreva block, described above, indicates that compressional deformation, at least at the foot of the volcanic edifice, occurred over a long period of time. The fact that only some sediment layers within the toreva block show westward thinning may indicate that deformation occurred episodically rather than continuously, similar to the Hilina Pali slump. The presence of a subtle thrust fold in areas evacuated during the catastrophic collapse indicate that spreading along the deep slide surface continued even during the last stage of the flank collapse (Fig. 6).

Ritter is very young and small compared to most other volcanoes affected by gradual flank spreading. Apart from the volcanic layering there are no indications for internal heterogeneities (e.g. old slide scarps) in the seismic data that would suggest that Ritter was predisposed to failure on the western flank, or to explain gradual spreading in this direction. Analogue models indicate that detachment surfaces within volcanic edifices may form solely due to gravitational instabilities (Delcamp et al., 2008), which is a plausible cause for gradual spreading within Ritter's edifice as it mainly consists of poorly consolidated, coarse volcaniclastic, and thus rather unstable material. Dyke intrusions often trigger episodic flank movements along deep-seated detachment surfaces (Bonforte et al., 2013). This process may also be relevant at Ritter, because the chain of parasitic cones, which have grown on top of young sediments on the southern slope of Ritter (F**igs. 2A, 3**), reveal relatively recent intrusion of magma perpendicular to the direction of sector displacement and thus provides a possible additional driver for the deep-seated deformation.

349 The slide surface of the catastrophic phase of the Ritter Island collapse is still preserved in the
350 bathymetry of the volcanic edifice and continues via the chutes either side of the toreva block, cutting
351 into the deformed seafloor sediments (**Figs. 4-6).** The geometry of the slide surface indicates that the
352 catastrophic collapse did not occur along the pre-existing shear zone associated with the deep-seated
353 flank instability but shallower. The erosional channels from the catastrophic collapse cut through the
354 well-developed folds (**Figs. 4, 5**), which indicates that the compression must predate the passage of
355 the mass flow derived from the catastrophic collapse phase. The relative timescales of these two
356 processes cannot be definitively constrained. Gradual compressional deformation may have extended
357 for many kilometers west of the growing Ritter edifice (alongside that observed at the foot of the
358 western flank, in the toreva block), but it is also possible that some of this compression occurred more
359 rapidly during an initial phase of the 1888 event, prior to and perhaps precipitating the catastrophic
360 collapse and disintegration of the upper part of the edifice.

361

362 **5.2. Catastrophic destruction of the volcanic cone**

363 Eyewitness tsunami observations of a single wave train and numerical landslide-tsunami simulations
364 indicate that the catastrophic collapse of Ritter must have been a fast and highly energetic event
365 occurring as a single phase of movement (Ward & Day, 2003). The hummocky terrain west of Ritter
366 has previously been interpreted as the debris avalanche deposit associated with this collapse (Johnson
367 1987; Day et al., 2015). However, the 3D seismic data reveal that these hummocks consist of
368 compressed seafloor sediments (**Figs. 4-6**), which have been deeply eroded by a highly energetic
369 flow, and not of large blocks transported within a chaotic matrix as observed at other submarine sector
370 collapse deposits (e.g., Montserrat; Crutchley et al., 2013). The absence of any large cone fragments
371 within the extent of the 3D seismic cube and the pronounced erosion of pre-existing sediments
372 suggest that the failed cone of Ritter disintegrated rapidly and transformed into a highly energetic and
373 mobile mass with a high proportion of relatively fine sediment. The erosional channels initiate next to
374 the scoria cone in front of the western flank of Ritter and carve continuously deeper into the
375 underlying compressed seafloor sediments as distance from Ritter increases (**Fig. 2**). Basal erosion

intensified when the sliding material was focused into a constriction formed by the volcanic ridges and cones (**Fig. 8C**). It is unclear how much of the disintegrative mass was deposited in the proximal region (our observations and samples indicate cobble- to sand-sized volcanic deposits across this region), but any such deposits are likely to be relatively thin and surficial, as there is no seismic indication for a layer on top of the deformed seafloor sediments. It is possible that more substantial volumes of the disintegrated mass were deposited in the north of the basin, infilling irregularities and leading to the relatively smooth surfaced seafloor here, but we nevertheless conclude that the majority of the 2.4 km^3 bypassed the proximal region.

For most of the over 400 identified volcanic sector collapses worldwide, the preconditions and trigger mechanisms are unknown (Siebert 1987). Ritter offers a rare opportunity to reconstruct the evolution of such an event, which may be triggered by a combination of various processes, such as over-steepening, tectonic earthquakes, magmatic intrusions and eruptions, but also by deep-seated gradual spreading (van Wyk de Vries & Francis, 1997; Carrasco-Núñez et al., 2011). As discussed above, deep-seated gradual spreading likely preconditioned the collapse of Ritter by inducing strain and continuous shearing. This shearing is reflected in the development of the two separate chutes. In addition to this preconditioning, a further mechanism may have initiated the transition from gradual spreading to catastrophic collapse. The detailed eyewitness accounts do not report any regionally felt earthquakes (Anonymous, 1888; Steinhäuser, 1892), which is a common trigger for catastrophic sector collapses (e.g. 1980 Mount St. Helens or the 1792 Unzen collapses; Siebert et al., 1987). However, a local tectonic event near or within the edifice of Ritter may not have been detected in settlements more than 100 km away. Therefore, moderate ground motion due to an earthquake remains a plausible trigger for the catastrophic phase of the 1888 Ritter sector collapse.

Many sector collapses are accompanied by explosive eruptions, leading to highly complex deposits (e.g. Hunt et al., 2017), and often it is difficult to reconstruct the temporal relationship between the mass movement and eruption. For Ritter, there are multiple independent observations indicating that explosive activity accompanied or was initiated by the rapid final phase of failure. Firstly, eyewitness accounts report a shot-like noise 40 minutes before the tsunami arrival in Hatzfeldhaven, ash fall and

403 washed-up pumice at multiple locations and steam emissions (presumably from the sea surface)
404 immediately after the collapse (Anonymous, 1888; Steinhäuser, 1892; Johnson, 2015). Secondly, the
405 seismic data reveal a depression in the center of the volcanic edifice, which has been filled by the
406 post-1888 cone (**Fig. 3**) and most likely represents an explosion crater. Ritter was frequently active
407 before 1888, and it is likely that incipient failure cut an active hydrothermal system above the conduit,
408 and that ingress of seawater during collapse would have generated a phreatic explosive eruption,
409 explaining both reports of detonations and potentially a source of ash generation (cf. the Bandai
410 collapse, 1888). Phreatic activity would explain the observation of post-collapse steam emissions and
411 local observation of pumice and ash deposition are more consistent with a magmatic eruption (cf.
412 Watt et al., 2019). We also note that more distal reports of ashfall and pumice in Kalena and
413 Finschhafen are harder to explain without a high eruption column, which is not supported by more
414 proximal observations.

415 The combined observations suggest that the catastrophic collapse of Ritter's cone in 1888 was likely
416 preconditioned by the interplay between gravitational spreading causing differential deformation and
417 structural weakening of the western flank and the episodic intrusion of magmatic dykes. We propose
418 that the long-term displacement and dissection destabilized the flank and that a local tectonic event or
419 the intrusion of magma triggered the catastrophic collapse. A triggered phreatic explosion, potentially
420 followed by magmatic eruption, provides an additional mechanism that may have facilitated
421 disintegration of the failing sector and accelerated the slide mass that allowed it to erode deeply into
422 the previously deformed seafloor sediments.

423

424 ### 5.3. Implications for interpreting debris avalanche deposits and tsunami hazard assessment

425 Tsunami genesis by a submarine landslide is primarily controlled by the volume and velocity of the
426 sliding mass and whether it is emplaced at once or in separate stages (Løvholt et al., 2005; Watt et al.,
427 2012). For Ritter, our data indicate that most of the material affected by the 1888 collapse (and by the
428 preceding, potentially long-term compressional deformation) consisted of deformed and eroded
429 seafloor material. Since this deformation involved limited lateral transport or vertical displacement,

and was probably gradual, it is unlikely to have contributed significantly to the 1888 tsunami. The incorporation and deformation of significant amounts of basement material resembles other sector collapse deposits studied onshore. Field geological mapping of the Socompa sector collapse in Chile indicated a total debris avalanche volume of ~25 km³ (excluding intact toreva blocks; van Wyk de Vries et al., 2001). Road cuts through this material show that 80% of this volume consists of entrained basement material and only a comparatively thin cover of material derived from the edifice collapse. While these onshore interpretations build on limited direct observations, we can quantify the volumes of different units of the Ritter sector collapse and their deposits as follows:

- Pre-collapse cone (fully evacuated from source region): ~2.4 +/-0.2 km³; volume reconstruction from bathymetry and historic reports
- Deformed seafloor material: ~11 +/- 1 km³ (including the toreva block; a small proportion of this volume may also comprise deposits from the disintegrated pre-collapse cone); volume estimate from seismic data
- Eroded seafloor sediments (proximal): ~1.6 +/- 0.1 km³; volume estimate from 3D seismic data
- Distal turbidites and debris flow units: ~5 km³ (Watt et al., 2019)

The first three estimates suggest that gradual spreading during the initial phase of slope instability affected about ~15 km³ (i.e. the deformed and eroded seafloor sediments and the cone), while the rapid, catastrophic phase of collapse only affected 2.4 km³ of the edifice. The material eroded from the channel network, with the missing pre-collapse cone volume, adds up to 4 km³. Some of this material was deposited in the basin west of Ritter, implying that at least a further 2 km³ of seafloor sediments was eroded further west, to account for the 6.4 km³ of material within distal turbidites and debris flow deposits Watt et al., 2019).

The instability and eventual collapse of Ritter's western flank therefore mobilized a total volume of at least 16 km³ of material, but this involved a wide variety of processes, velocities and extents of lateral transport. As little as 15% of this volume (2.4 km^3, with a possible additional translational movement of deeper material, such as that in the toreva block) formed the primary, rapidly moving collapse

457 mass, and was thus the tsunamigenic component of the event. These results differ from previous
458 estimates based solely on bathymetric mapping, which resulted in a volume of 4.2 km³ for the primary
459 collapse, 6.4 km³ for the distal deposits including incorporated seafloor sediments, and a total volume
460 of about 10 km³ (Day et al., 2015). The differences between Day et al. (2015) and our volume
461 estimates highlight the difficulties of interpreting mass-movement deposits solely from surface
462 morphologies and the importance of subsurface geometry constraints by seismic data in landslide
463 volume calculations. The previous estimates were biased on interpreting the proximal Ritter deposit as
464 the block-rich facies of a debris avalanche and inferring that the hummocky terrain comprised large
465 fragments of the failed cone, transported within a matrix of chaotic material. In contrast, our internal
466 imaging shows that the deposits proximal to Ritter are dominated by compressional structures (**Fig.**
467 **4**), and that the hummocks west of Ritter consist of deformed seafloor sediments that were
468 morphologically modified by erosion. In this sense, the hummocky morphology at Ritter differs from
469 what is typically interpreted within subaerial and many submarine volcanic debris avalanches. A
470 'blocky' seafloor morphology consequently may not always indicate a deposit of a primary landslide
471 mass, but could also result from the complex combination of deformation and erosion.

472 Our estimate that the rapidly-moving landslide mass accounted for just 15% of the total volume of the
473 Ritter deposit is comparable to estimates of the primary edifice to basement ratio within the Socompa
474 deposits, and exceeds the estimates for the sediment-rich volcanic-collapse deposits offshore
475 Montserrat, where seafloor material contributes half or two-thirds of the entire deposit volume (Watt
476 et al., 2012). By distinguishing between gradual deformation and catastrophic failure, the volume of
477 the rapidly moving phase of the Ritter collapse (2.4 km^3) may have been even smaller than the 2.7
478 km³ calculated for the 1980 Mount St. Helens sector collapse using a similar approach (Moore &
479 Albee, 1981), which questions whether the 1888 Ritter sector collapse should be classified as the
480 largest historic sector collapse.

481 Previous numerical tsunami simulations reproduced the historic tsunami observations quite
482 convincingly using a slide volume of 4.6 km³ and a slide emplacement velocity of 40 m/s (Ward and
483 Day, 2003). However, the solely bathymetrically constrained volume calculations overestimated the

484 rapidly moving (and tsunamigenic) collapse volume by 75% compared to our seismically constrained
485 estimates. This implies that the collapsing mass of Ritter must either have had a higher velocity than
486 previously assumed or that additional processes amplified the tsunami wave. The potential explosion
487 during the collapse of Ritter may have had an influence on the disintegration and mobility of the
488 sliding mass or even contributed directly to tsunami genesis by the displacement of water, as shown
489 for the 1650 submarine explosive eruption of Kolumbo volcano in the Aegean Sea (Ulvrova et al.,
490 2016). Any landslide-tsunami simulations that treat the sliding mass as gravitationally accelerated
491 blocks or fluids, cannot address this complexity (Løvholt et al, 2015). This highlights the need for
492 advanced numerical simulations and improved source mechanism parameterization to achieve more
493 reliable volcanogenic tsunami hazard assessments.

494

495 ## 6. Conclusions

496 The 3D seismic analysis of the remnants of the Ritter Island volcanic cone and the adjacent deposits
497 indicates that the sector collapse of Ritter occurred in two stages (**Fig. 9**). The initial phase was
498 characterized by deep-seated gradual spreading potentially controlled by extension within the volcanic
499 edifice. The gradual spreading developed over a long period of cone growth and resulted in
500 compressional deformation within the volcanic edifice of Ritter. A pre-existing scoria cone buttressed
501 the central segment of the western flank, induced shearing within the mobile flank, and explains the
502 presence of the preserved toreva block. The seafloor sediments at the base of Ritter's western flank
503 show pronounced compression, which developed either simultaneously with the deformation in the
504 toreva block or during the early stages of the catastrophic collapse itself. The second phase of the
505 collapse was highly energetic and led to disintegration of 2.4 km^3 of the Ritter cone in 1888. The
506 failed cone formed an erosive mass flow that cut deeply into the previously deformed seafloor
507 material and formed erosional channels and a hummocky inter-channel morphology within the basin
508 west of Ritter. Historic eyewitness accounts and a crater-like depression within the volcanic edifice
509 suggest that the collapse was likely accompanied by an explosive phreatic, and possibly magmatic,

510 eruption (**Fig. 9**). The collapse was most probably triggered by a local tectonic event or the intrusion
511 of magma into the volcanic edifice, but this inference remains speculative without further data.

512 The entire Ritter Island failure affected ~11 km³ of proximal basin-filling sediments, which is far
513 more voluminous than the final catastrophic collapse of the cone itself, which had a volume of ~2.4
514 km³. Our analyses suggest that only this final collapse was responsible for the devastating tsunami,
515 and indicate that only 15% of the total mass-transport deposit contributed to tsunami genesis. These
516 observations highlight the importance of high-resolution geophysical subsurface data to reliably
517 reconstruct volcanic landslide emplacement parameters, which are crucial for reliable geohazards
518 assessments. Without such constraints, tsunamigenic slide volumes may be systematically
519 overestimated. Our results show that volcanic eruptions accompanying volcanic sector collapses have
520 the potential to significantly change the dynamics of the travelling mass and therefore require special
521 attention in future landslide-tsunami simulations.

522

523 **Acknowledgements**

524 We dedicate this research to the memory of co-author Melanie Ray, who made significant
525 contributions to this research and to a much wider body of work on Ritter Island. As a valued member
526 of the SO252 science team, Melanie's work was important for many of the interpretations presented
527 here. The German Ministry of Science and Education (BMBF) funded this study through the "Ritter
528 Island project" (03G0252A). We thank the master and the crew of the RV Sonne for their support
529 during research cruise SO252. We would like to thank Schlumberger and IHS for granting educational
530 licenses. AM is funded by the European Research Council under the European Union's Horizon 2020
531 Programme (grant agreement n° 677898).

Figures

Fig. 1: A) Tectonic framework of the Bismarck Sea with major structural element (BSSL: Bismarck Sea seismic lineation; based on Baldwin et al., 2012. B) Topographic map of the study area between New Britain, Umboi, Sakar and Ritter with data coverage from research cruise SO252, GEBCO and Aster digital elevation model grids. C) Shaded relief map of the study area with extent of P-Cable 3D seismic cube and seismic profiles presented in this study.

Fig. 2: A) 3D view on the failed volcanic cone of Ritter (all 3D views are 3 times vertically exaggerated). B) 3D view on the hummocky 1888 Ritter collapse deposits with erosional channels and pre-1888 volcanic cones. Seafloor photography of C) exposed lava at the collapse scarp, D) sheeted lava flows, E) fine grained sediments within an erosional channel and F) scoria pebbles of the volcanic cone west of Ritter. G) 3D view on the failed volcanic cone of Ritter towards the neighboring basin filled with 1888 collapse deposits. H) 3D view on the hummocky 1888 Ritter collapse deposits with erosional channels, pre-1888 volcanic cones. Letters in red circles indicate location of seafloor photographs in the corresponding figure panels.

Fig. 3: 2D seismic profile crossing the intact and failed parts of Ritter revealing the internal architecture of the volcanic edifice, the post-1888 volcanic cone grown on top of a crater-like depression and several parasitic cones.

Fig. 4: A) and B) Seismic profiles from the 3D seismic dataset revealing the internal architecture of the deformed and eroded sediments including folded sediment packages, rotated blocks, and shear zones as well as the interaction with pre-collapse volcanic cones and ridges.

Fig. 5: A) and B) Seismic profiles from the 3D seismic dataset revealing the internal architecture of the deformed and eroded sediments including folded sediment packages, rotated blocks, and shear zones as well as the interaction with pre-collapse volcanic cones and ridges.

Fig. 6: 3D seismic view on the deformed sediments within and in front of the toreva block pushed on top of the neighboring scoria cone. A continuous seismic reflection within the toreva block is traced in 3D (purple) and a thrust fault coinciding with a sediment ridge is marked with arrows.

Fig. 7) A) Seismic profile showing deformed sediment layers within the toreva block indicating an increased deformation with depth. B) Comparison between contour lines of the toreva block with the specific contour lines from the cone reconstruction indicating the lateral displacement of the toreva block.

Fig. 8: A) 3D view on Ritter and the surrounding seafloor with a reconstruction of the pre-collapse cone B) Thickness map of the sediments affected by the failure of Ritter calculated with a seismic velocities of 1500 m/s. C) Thickness map of the eroded sediments by the failure of Ritter.

Fig. 9: Reconstruction of the 1888 Ritter sector collapse

571 **References**

572 1. Anonymous, 1888. Die Fluthwelle vom 13. Maerz 1888. Nachrichten über Kaiser Wilhelms-
573 Land und den Bismarck-Archipel, 4(3),147-149.
574 2. Auker, M. R., Sparks, R. S. J., Siebert, L., Crosweller, H. S., Ewert, J., 2013. A statistical
575 analysis of the global historical volcanic fatalities record. *Journal of Applied*
576 *Volcanology*, *2*(1), 2.
577 3. Baldwin, S.L., Fitzgerald, P.G., Webb, L.E., 2012. Tectonics of the New Guinea Region.
578 Annual Review of Earth and Planetary Sciences 40, 495-520.
579 4. Barnes, P. M., Ghisetti, F. C., Ellis, S., & Morgan, J. K., 2018. The role of protothrusts in
580 frontal accretion and accommodation of plate convergence, Hikurangi subduction margin,
581 New Zealand. Geosphere, 14(2), 440-468.
582 5. Bonforte, A., Guglielmino, F., Puglisi, G., 2013. Interaction between magma intrusion and
583 flank dynamics at Mt. Etna in 2008, imaged by integrated dense GPS and DInSAR data.
584 Geochem. Geophys. Geosyst. 14, 2818–283.
585 6. Carrasco-Núñez, G., Siebert, L., Capra, L., Veress, B., Szigethy, J., 2011. Hazards from
586 volcanic avalanches. Horizons in Earth Science Research, 3, 199-227.
587 7. Casalbore, D., Romagnoli, C., Chiocci, F., Frezza, V., 2010. Morpho-sedimentary
588 characteristics of the volcaniclastic apron around Stromboli volcano (Italy). Marine Geology,
589 269(3-4), 132-148.
590 8. Cunningham, H., Gill, J., Turner, S., Caulfield, J., Edwards, L., Day, S., 2012. Rapid
591 magmatic processes accompany arc-continent collision: the Western Bismarck arc, Papua
592 New Guinea. Contributions to Mineralogy and Petrology 164, 789-804.
593 9. Crutchley, G. J., Karstens, J., Berndt, C., Talling, P. J., Watt, S. F. L., Vardy, M. E.,
594 Hühnerbach, V., Urlaub, M., Sarkar, S., Klaeschen, D., Paulatto, M., Le Friant, A., Lebas, E.,
595 Maeno, F., 2013. Insights into the emplacement dynamics of volcanic landslides from high-
596 resolution 3D seismic data acquired offshore Montserrat, Lesser Antilles. Marine Geology,
597 335, 1-15.

598 10. Day, S. J., Da Silva, S. H., Fonseca, J. F. B. D., 1999. A past giant lateral collapse and
599 present-day flank instability of Fogo, Cape Verde Islands. Journal of Volcanology and
600 Geothermal Research, 94(1-4), 191-218.
601 11. Day, S. J., Ward, S., 2003. Ward, S. N., & Day, S. (2003). Ritter Island volcano—lateral
602 collapse and the tsunami of 1888. Geophysical Journal International, 154(3), 891-902.
603 12. Day, S. J., 2015. Chapter 58 - Volcanic Tsunamis, In The Encyclopedia of Volcanoes
604 (Second Edition), edited by Haraldur Sigurdsson, Academic Press, Amsterdam, 2015, Pages
605 993-1009, ISBN 9780123859389.
606 13. Day, S. J., Llanes, P., Silver, E., Hoffman, G., Ward, S., Dricoll, N., 2015. Submarine
607 landslide deposits of the historical lateral collapse of Ritter Island, Papua New Guinea.
608 Marine and Petroleum Geology 67, 419-438.
609 14. Delcamp, A., van Wyk de Vries, B.“ & James, M. R., 2008. The influence of edifice slope and
610 substrata on volcano spreading. Journal of Volcanology and Geothermal Research, 177(4),
611 925-943.
612 15. Dufresne, A., Salinas, S., Siebe, C., 2010. Substrate deformation associated with the
613 Jocotitlán edifice collapse and debris avalanche deposit, Central México. Journal of
614 Volcanology and Geothermal Research, 197(1-4), 133-148.
615 16. Denlinger, R. P., Okubo, P., 1995. Structure of the mobile south flank of Kilauea Volcano,
616 Hawaii. Journal of Geophysical Research: Solid Earth, 100(B12), 24499-24507.
617 17. Deplus, C., Le Friant, A., Boudon, G., Komorowski, J. C., Villemant, B., Harford, C.,
618 Ségoufin, J., Cheminée, J. L., 2001. Submarine evidence for large-scale debris avalanches in
619 the Lesser Antilles Arc. Earth and Planetary Science Letters, 192(2), 145-157.Gase et al.,
620 2017
621 18. Glicken, H., 1996. Rockslide-debris avalanche of May 18, 1980, Mount St. Helens Volcano,
622 Washington (No. 96-677). US Geological Survey.
623 19. Fujie, G., Kasahara, J., Murase, K., Mochizuki, K., Kaneda, Y., 2008. Interactive analysis
624 tools for the wide-angle seismic datafor crustal structure study (Technical Report), in
625 Exploration Geophysics, 39(1), 26-33.

626 20. Holm, R.J., and Richards, S.W., 2013, A re-evaluation of arc-continent collision and along-
627 arc variation in the Bismarck Sea region, Papua New Guinea. Australian Journal of Earth
628 Sciences 60, 605-619.
629 21. Johnson, R.W., 1977. Distribution and major-element chemistry of late Cainozoic volcanoes
630 at the southern margin of the Bismarck Sea, PNG. Australian Bureau of Mineral Resources,
631 Geology and Geophysics Report 188, 162 pp.
632 22. Johnson, R.W., 1987. Large scale volcanic cone collapse: the 1888 slope failure of Ritter
633 volcano. Bulletin of Volcanology 49, 669-679.
634 23. Johnson, R.W., 2013. Fire Mountains of the Island: a history of volcanic eruptions and
635 disaster management in Papua New Guinea and the Solomon Islands. Australian National
636 University Press, 416 pp.
637 24. Karstens, J., Crutchley, G. J., Berndt, C., Talling, B. J., Watt, S. F. L., Hühnerbach, V., Le
638 Friant, A., Lebas, E., Trofimovs, J., 2013. Emplacement of pyroclastic deposits offshore
639 Montserrat from 3D seismic data Journal of Volcanology and Geothermal Research, 257 . pp.
640 1-11. DOI 10.1016/j.jvolgeores.2013.03.004.
641 25. Løvholt, F., Harbitz, C. B., Haugen, K. B., 2005. A parametric study of tsunamis generated by
642 submarine slides in the Ormen Lange/Storegga area off western Norway. Marine and
643 Petroleum Geology, 22(1), 219-231.
644 26. Løvholt, F., Pedersen, G., Harbitz, C. B., Glimsdal, S., Kim, J., 2015. On the characteristics
645 of landslide tsunamis. Phil. Trans. R. Soc. A, 373(2053), 20140376.
646 27. Masson, D. G., Watts, A. B., Gee, M. J. R., Urgeles, R., Mitchell, N. C., Le Bas, T. P.,
647 Canals, M., 2002. Slope failures on the flanks of the western Canary Islands. Earth-Science
648 Reviews, 57(1), 1-35.
649 28. McMurtry, G. M., Watts, P., Fryer, G. J., Smith, J. R., Imamura, F., 2004. Giant landslides,
650 mega-tsunamis, and paleo-sea level in the Hawaiian Islands. Marine Geology, 203(3), 219-
651 233.

29. Moore, J. G., Albee, W. C., Lipman, P. W., & Mullineaux, D. R., 1981. Topographic and structural changes, March-July 1980—Photogrammetric data. The 1980 Eruptions of Mount St. Helens, Washington, 1250, 123-134.
30. Moore, J. G., Clague, D. A., Holcomb, R. T., Lipman, P. W., Normark, W. R., Torresan, M. E. 1989. Prodigious submarine landslides on the Hawaiian Ridge. Journal of Geophysical Research: Solid Earth, 94(B12), 17465-17484.Morgan et al, 2003
31. Murray, J. B., van Wyk de Vries, B. Pitty, A., Sargent, P., & Wooller, L., 2018. Gravitational sliding of the Mt. Etna massif along a sloping basement. Bulletin of Volcanology, 80(4), 40.
32. Paris, R., Bravo, J. J. C., González, M. E. M., Kelfoun, K., Nauret, F., 2017. Explosive eruption, flank collapse and megatsunami at Tenerife ca. 170 ka. Nature Communications, 8.
33. Pope, E. L., Jutzeler, M., Cartigny, M. J., Shreeve, J., Talling, P. J., Wright, I. C., Wysoczanski, R. J., 2018. Origin of spectacular fields of submarine sediment waves around volcanic islands. Earth and Planetary Science Letters, 493, 12-24.
34. Ramalho, R. S., Winckler, G., Madeira, J., Helffrich, G. R., Hipólito, A., Quartau, R., Adena, K., Schaefer, J. M., 2015. Hazard potential of volcanic flank collapses raised by new megatsunami evidence. Science advances, 1(9), e1500456.
35. Roth, T., 2018. Lithological constraints from p-wave velocity modelling of OBS data in the northeast of Ritter Island (Bismarck Sea). Master thesis, Christian-Albrecht-Universität zu Kiel, 84 pp.
36. Saunders, S., and Kuduon, J., 2009. The June 2009 investigation of Ritter volcano, with a brief discussion on its current nature. Independent State of Papua New Guinea, Volcanological Observatory Open File Report 003/2009, 30 pp.
37. Siebert, L., 1984. Large volcanic debris avalanches: characteristics of source areas, deposits, and associated eruptions. Journal of volcanology and geothermal research, 22(3-4), 163-197.
38. Siebert, L., Glicken, H., Ui, T., 1987. Volcanic hazards from Bezymianny-and Bandai-type eruptions. Bulletin of Volcanology, 49(1), 435-459.

678 39. Silver, E., Day, S.J., Ward, S.N., Hoffmann, G., Llanes-Estrada, P., Driscoll, N., Appelgate,
679 B., Saunders, S., 2009. Volcano collapse and tsunami generation in the Bismarck volcanic
680 arc, Papua New Guinea. Journal of Volcanology and Geothermal Research 186, 210-222.
681 40. Smith, J. R., Malahoff, A., & Shor, A. N., 1999. Submarine geology of the Hilina slump and
682 morpho-structural evolution of Kilauea volcano, Hawaii. Journal of volcanology and
683 geothermal research, 94(1-4), 59-88.
684 41. Steinhäuser, R., 1892. Die Flutwelle und die Hilfsexpedition voll Finschhafen nach der
685 Südwestküste von Neu-Pommern. Westermanns Illustrierte deutsche Monatshefte, 71, pp.
686 265–75.
687 42. Ulvrova M., Paris R., Nomikou P., Kelfoun K., Leibrandt S., Tappin D.R., McCoy F.W.,
688 2016. Source of the tsunami generated by the 1650 AD eruption of Kolumbo submarine
689 volcano (Aegean Sea, Greece). J. Volc. Geotherm. Res. 321, 125–139.
690 43. Urlaub, M., Petersen, F., Gross, F., Bonforte, A., Puglisi, G., Guglielmino, F., Krastel, S.,
691 Lange, D., Kopp, H., 2018. Gravitational collapse of Mount Etna's southeastern flank.
692 Science advances, 4(10), eaat9700.
693 44. van Wyk de Vries, B., & Francis, P. W., 1997. Catastrophic collapse at stratovolcanoes
694 induced by gradual volcano spreading. Nature, 387(6631), 387.
695 45. van Wyk de Vries, B., Self, S., Francis, P. W., & Keszthelyi, L., 2001. A gravitational
696 spreading origin for the Socompa debris avalanche. Journal of Volcanology and Geothermal
697 Research, 105(3), 225-247.
698 46. Wadge, G., Francis, P. W., Ramirez, C. F. 1995. The Socompa collapse and avalanche event.
699 Journal of Volcanology and Geothermal Research, 66(1-4), 309-336.Ward, S. N., Day, S.,
700 2003. Ritter Island volcano—lateral collapse and the tsunami of 1888. Geophysical Journal
701 International, 154(3), 891-902.
702 47. Watt, S.F.L., Talling, P.J., Vardy, M.E., Heller, V., Hühnerbach, V., Urlaub, M., Sarkar, S.,
703 Masson, D.G., Henstock, T.J., Minshull, T.A., Paulatto, M., Le Friant, A., Lebas, E., Berndt,
704 C., Crutchley, G.J., Karstens, J., Stinton, A.J., Maeno, F., 2012. Combinations of volcanic-

705 flank and seafloor-sediment failure offshore Montserrat, and their implications for tsunami
706 generation. Earth and Planetary Science Letters, Vol. 319-320, pp. 228–240.
707 48. Watt, S.F.L., Talling, P.J., Hunt, J.E., 2014. New insights into the emplacement dynamics of
708 volcanic island landslides. Oceanography 27, 46-57
709 49. Waythomas, C. F., Watts, P., Shi, F., & Kirby, J. T., 2009. Pacific Basin tsunami hazards
710 associated with mass flows in the Aleutian arc of Alaska. Quaternary Science Reviews,
711 28(11-12), 1006-1019.

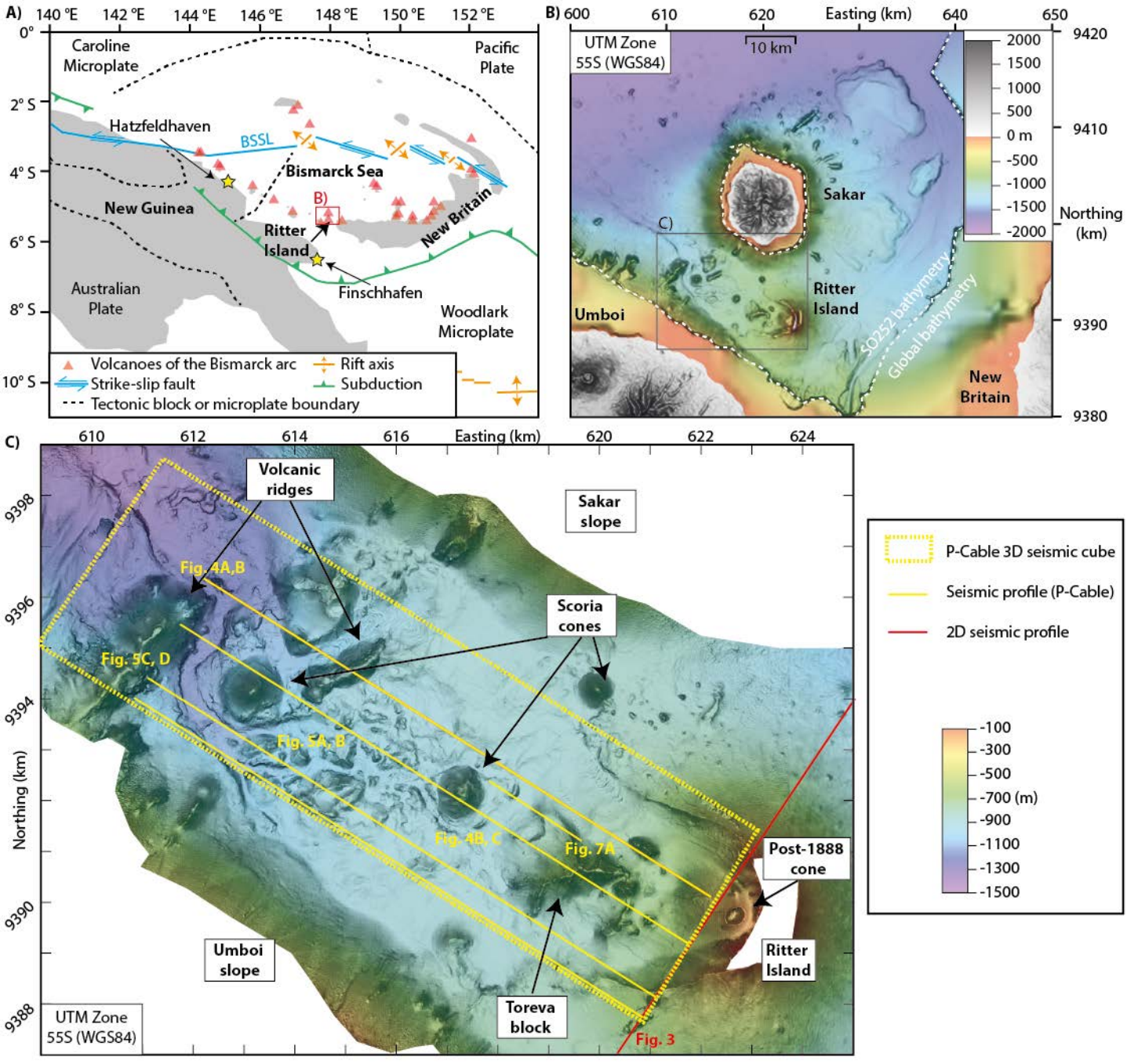
A)
140 °E
142 °E
144 °E
146 °E
148 °E
150 °E
152 °E
0°
2° S
4° S
6° S
8° S
10° S
Caroline Microplate
Pacific Plate
Hatzfeldhaven
BSSL
Bismarck Sea
New Guinea
B)
Ritter Island
New Britain
Finschhafen
Australian Plate
Woodlark Microplate
Volcanoes of the Bismarck arc
Strike-slip fault
Tectonic block or microplate boundary
Rift axis
Subduction
B)
600
610
620
Easting (km)
640
650
9420
9410
9390
9380
Northing (km)
UTM Zone 55S (WGS84)
10 km
2000
1500
1000
500
0 m
-500
-1000
-1500
-2000
Sakar
C)
Ritter Island
Umboi
SO252 bathymetry
Global bathymetry
New Britain
C)
610
612
614
616
Easting (km)
620
622
624
9398
9396
9394
9390
9388
Northing (km)
Volcanic ridges
Sakar slope
Fig. 4A,B
Scoria cones
Fig. 5C, D
Fig. 5A, B
Fig. 4B, C
Fig. 7A
Post-1888 cone
Umboi slope
Ritter Island
Toreva block
Fig. 3
UTM Zone 55S (WGS84)
P-Cable 3D seismic cube
Seismic profile (P-Cable)
2D seismic profile
-100
-300
-500
-700 (m)
-900
-1100
-1300
-1500

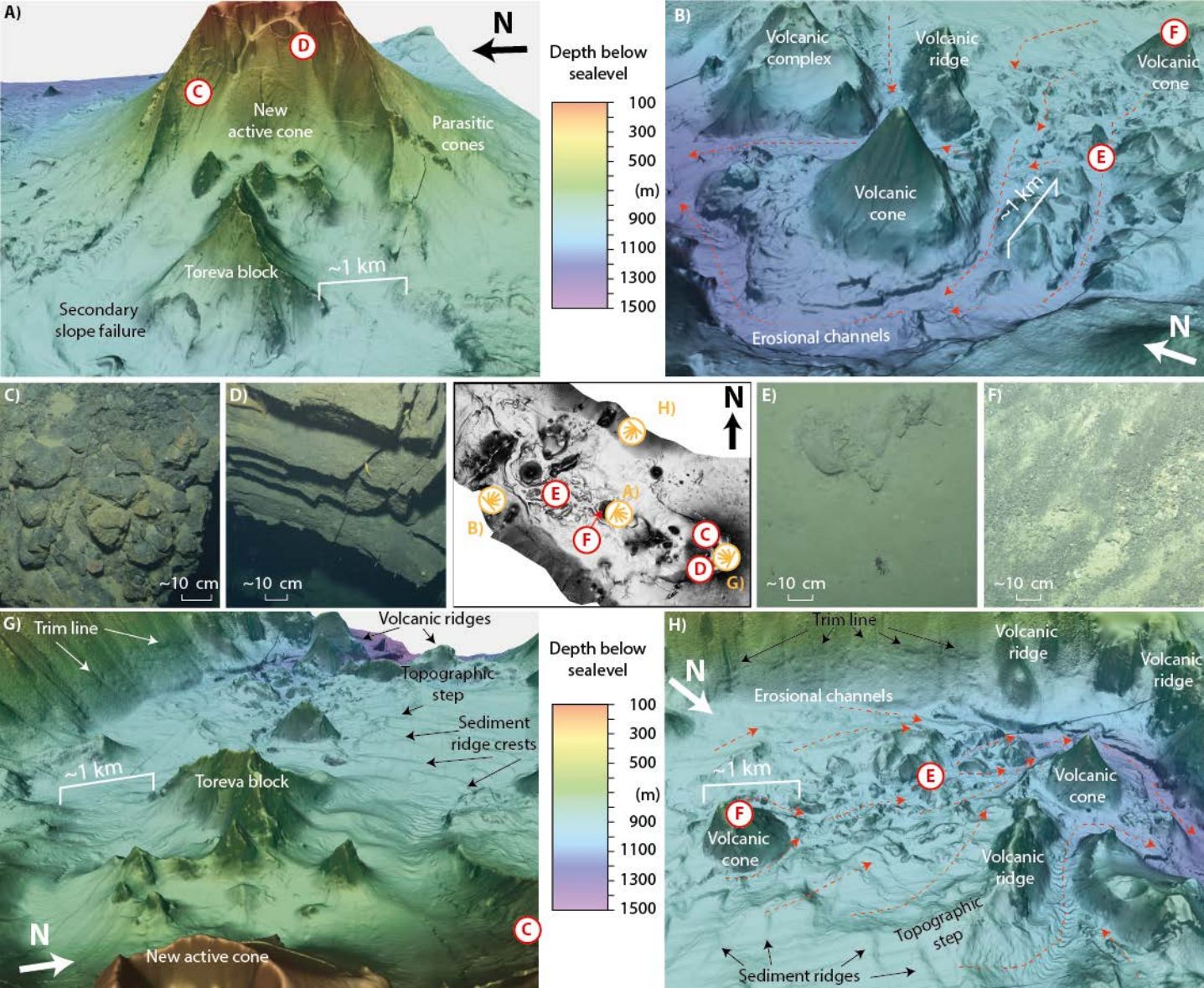
A)
N
D
C
New
active cone
Parasitic
cones
Toreva block
~1 km
Secondary
slope failure
Depth below
sealevel
100
300
500
(m)
900
1100
1300
1500
B)
Volcanic
complex
Volcanic
ridge
F
Volcanic
cone
E
Volcanic
cone
~1 km
Erosional channels
N
C)
~10 cm
D)
~10 cm
N
H)
E
A)
B)
F
C
D
G)
E)
~10 cm
F)
~10 cm
G)
Trim line
Volcanic ridges
Topographic
step
Sediment
ridge crests
~1 km
Toreva block
N
New active cone
C
Depth below
sealevel
100
300
500
(m)
900
1100
1300
1500
H)
Trim line
Volcanic
ridge
Volcanic
ridge
N
Erosional channels
~1 km
E
Volcanic
cone
F
Volcanic
cone
Volcanic
ridge
Topographic
step
Sediment ridges

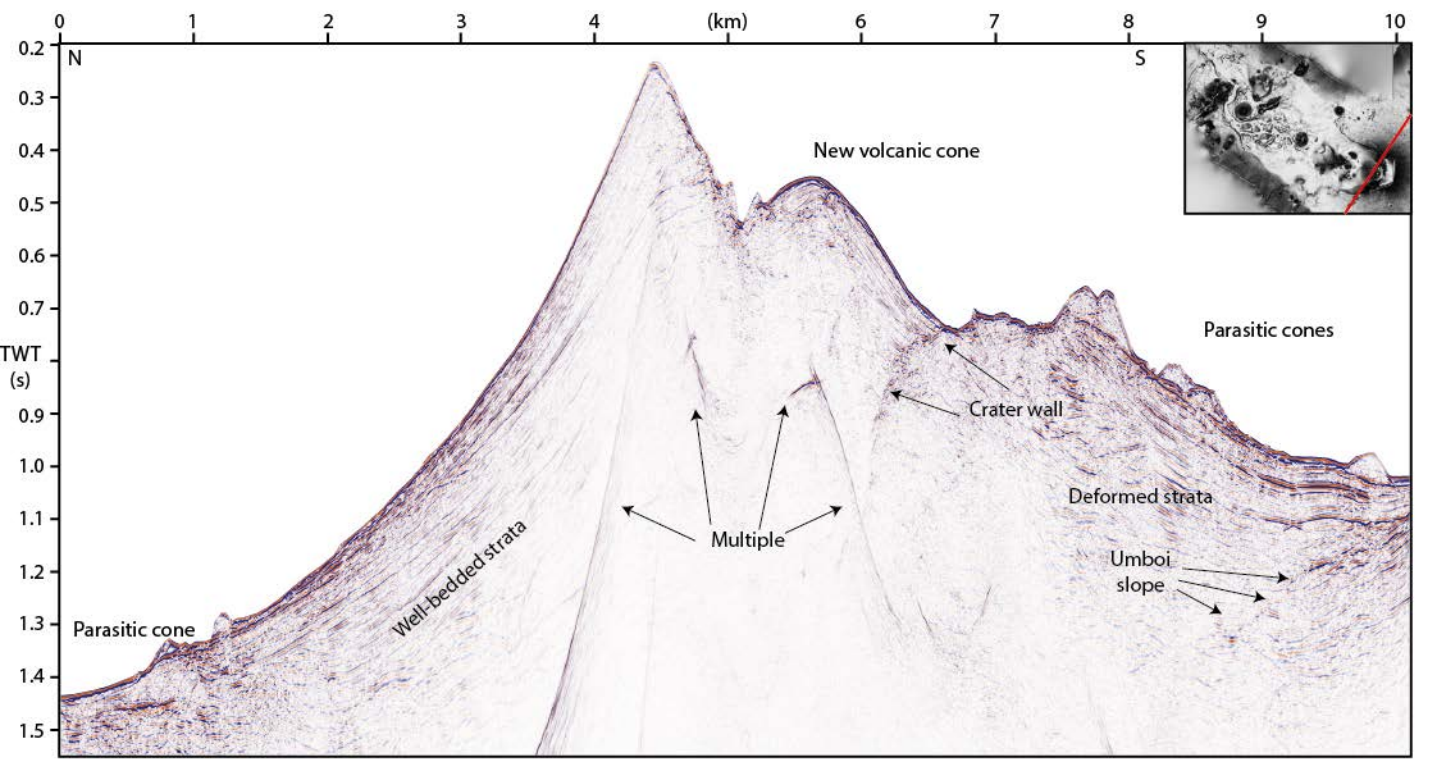
0
1
2
3
4
(km)
6
7
8
9
10
N
S
0.2
0.3
0.4
0.5
0.6
0.7
TWT
(s)
0.9
1.0
1.1
1.2
1.3
1.4
1.5
New volcanic cone
Parasitic cones
Crater wall
Deformed strata
Multiple
Umboi
slope
Parasitic cone
Well-bedded strata

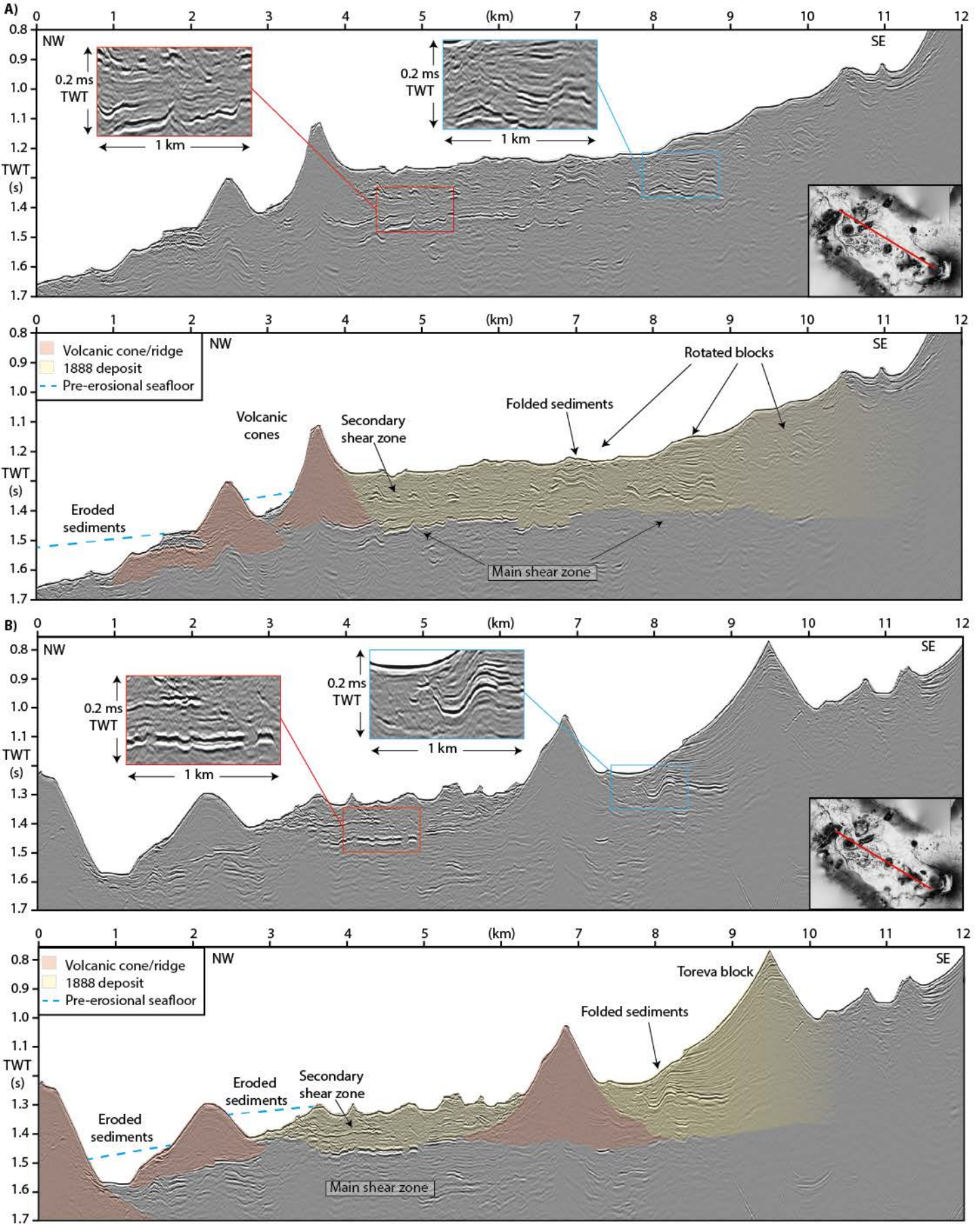
A)
NW
SE
0.2 ms TWT
1 km
0.2 ms TWT
1 km
TWT (s)
(km)
Volcanic cone/ridge
1888 deposit
Pre-erosional seafloor
Volcanic cones
Secondary shear zone
Folded sediments
Rotated blocks
Eroded sediments
Main shear zone
B)
NW
SE
0.2 ms TWT
1 km
0.2 ms TWT
1 km
TWT (s)
(km)
Volcanic cone/ridge
1888 deposit
Pre-erosional seafloor
Toreva block
Folded sediments
Eroded sediments
Secondary shear zone
Eroded sediments
Main shear zone

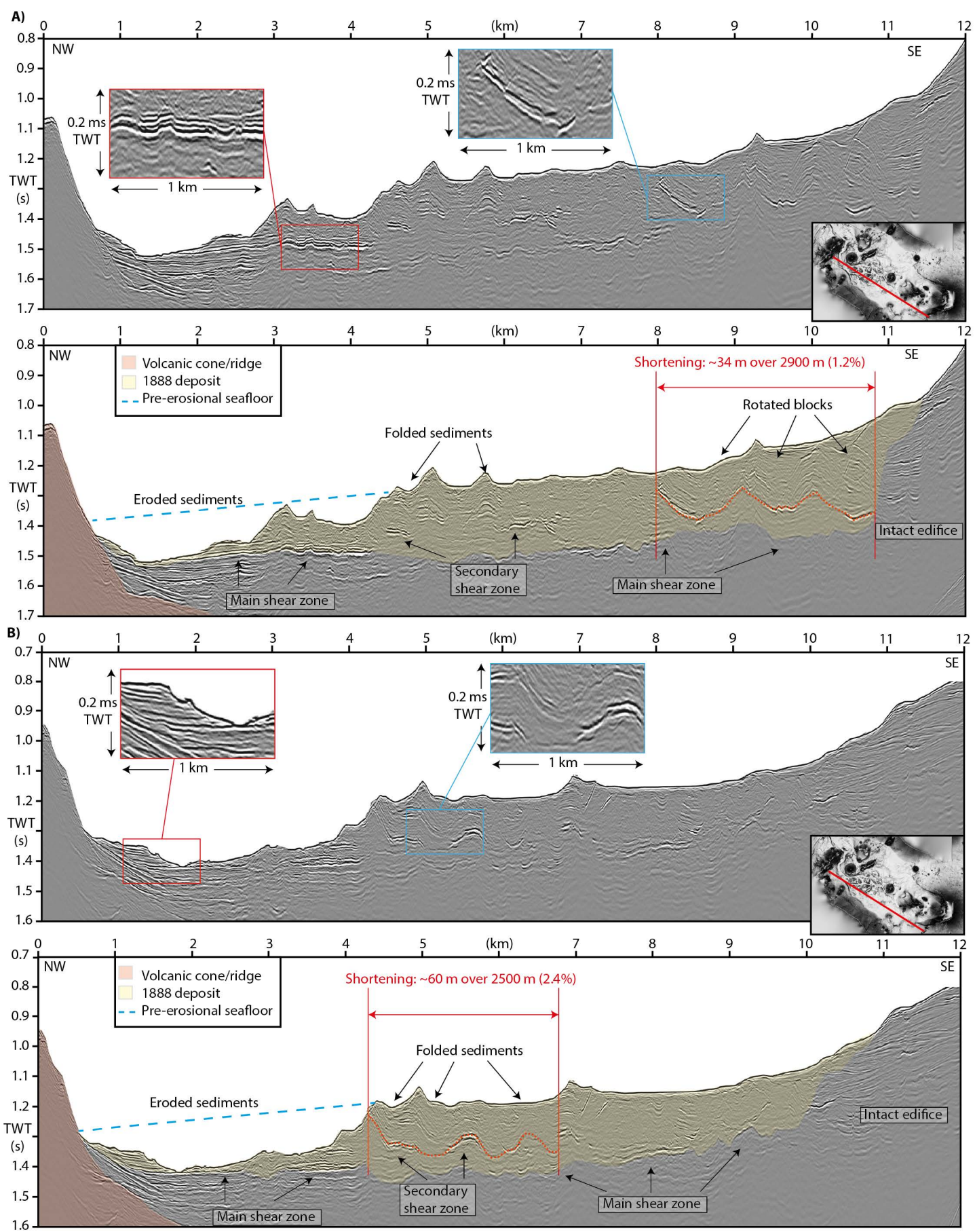
A)
NW
SE
0.2 ms TWT
1 km
0.2 ms TWT
1 km
TWT (s)
(km)
Volcanic cone/ridge
1888 deposit
Pre-erosional seafloor
Shortening: ~34 m over 2900 m (1.2%)
Rotated blocks
Folded sediments
Eroded sediments
Intact edifice
Secondary shear zone
Main shear zone
Main shear zone
B)
NW
SE
0.2 ms TWT
1 km
0.2 ms TWT
1 km
TWT (s)
(km)
Volcanic cone/ridge
1888 deposit
Pre-erosional seafloor
Shortening: ~60 m over 2500 m (2.4%)
Folded sediments
Eroded sediments
Intact edifice
Secondary shear zone
Main shear zone
Main shear zone

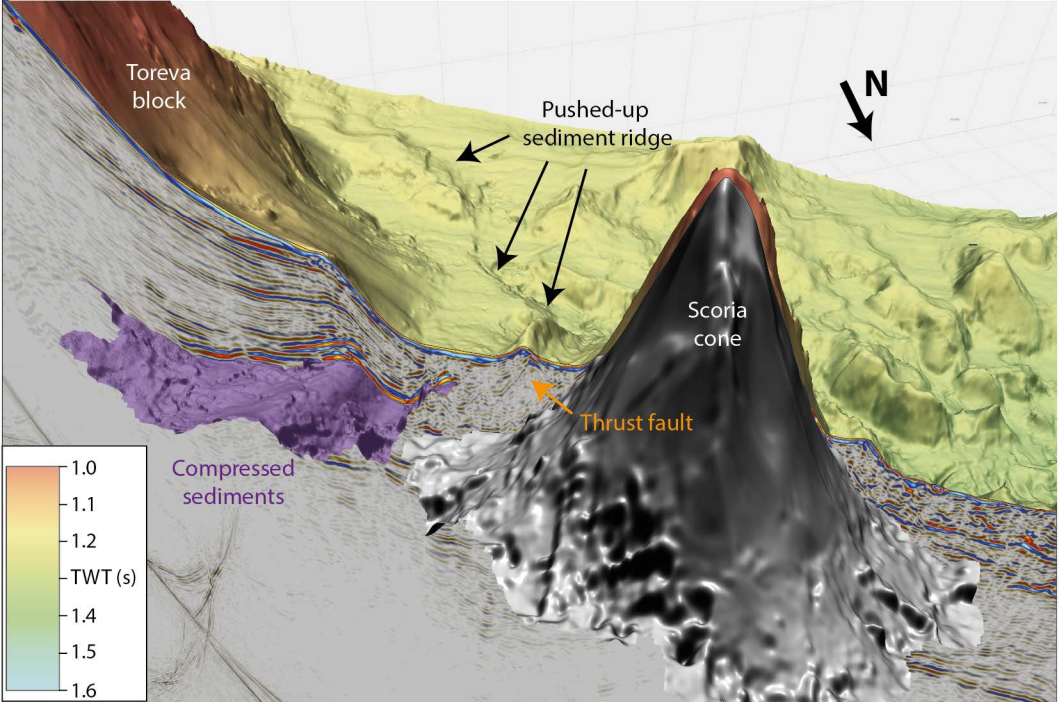
Toreva block
Pushed-up sediment ridge
N
Scoria cone
Thrust fault
Compressed sediments
1.0
1.1
1.2
TWT (s)
1.4
1.5
1.6

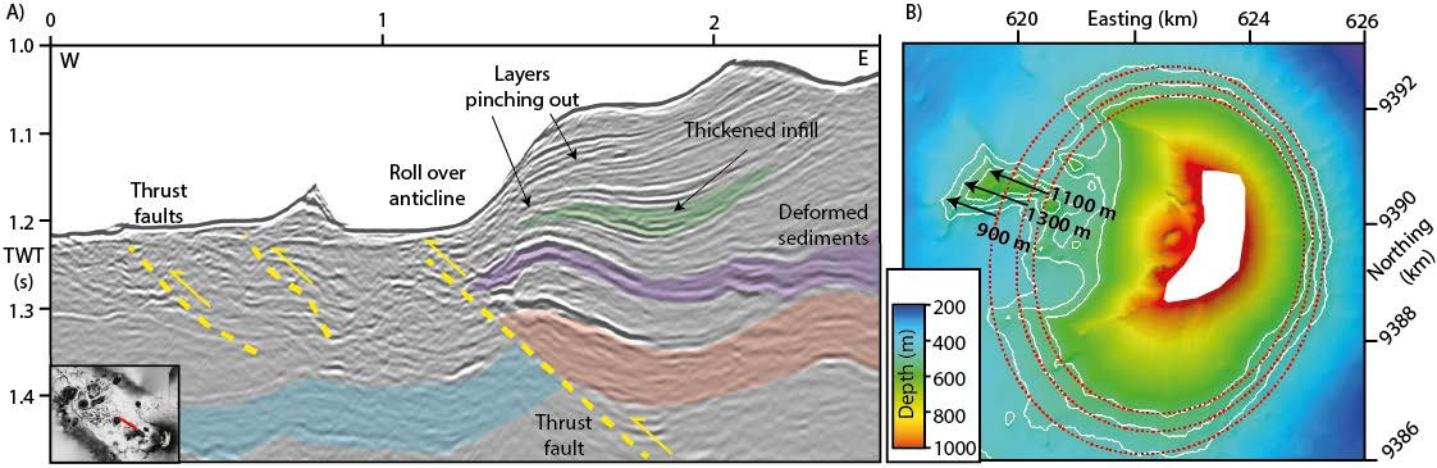
A)
0
1
2
1.0
1.1
1.2
1.3
1.4
TWT (s)
W
E
Layers pinching out
Thickened infill
Roll over anticline
Thrust faults
Deformed sediments
Thrust fault
B)
620
Easting (km)
624
626
9392
9390
9388
9386
Northing (km)
1100 m
1300 m
900 m
Depth (m)
200
400
600
800
1000

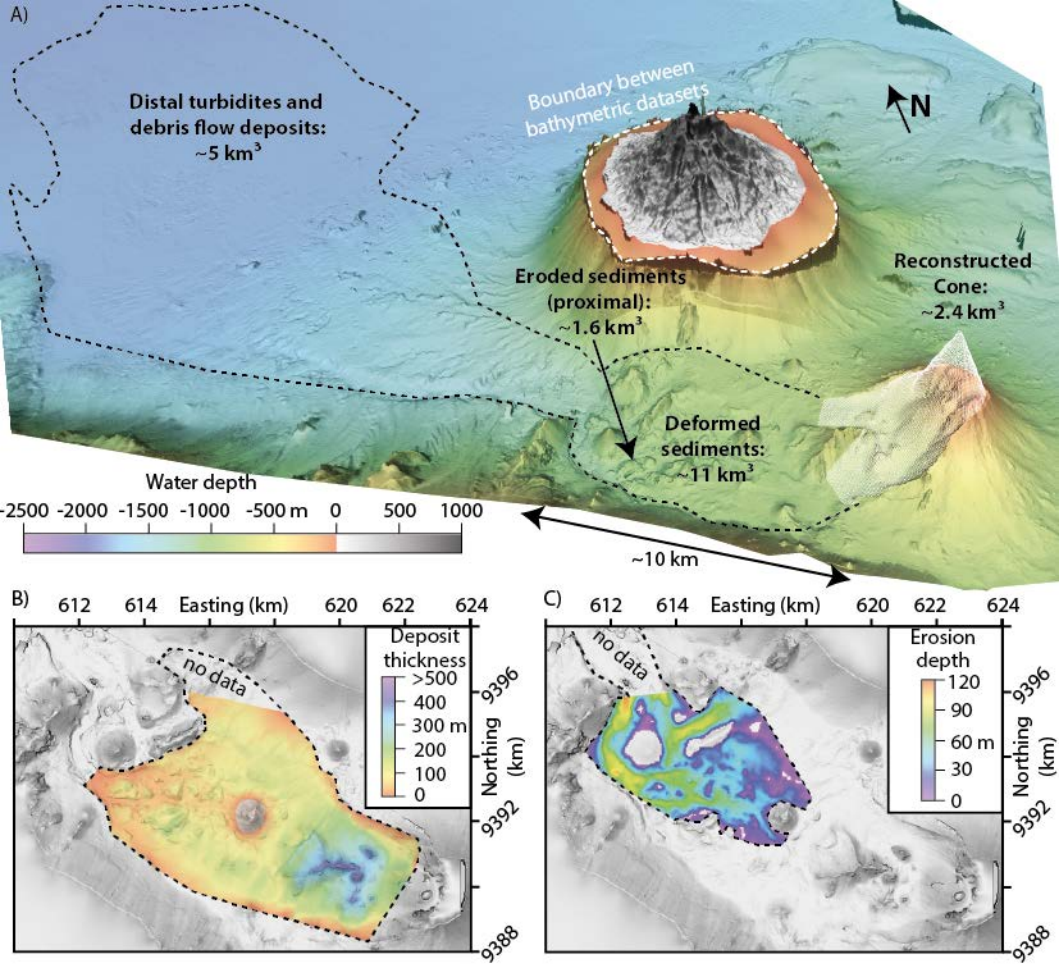
A)
Distal turbidites and debris flow deposits: ~5 km³
Boundary between bathymetric datasets
N
Eroded sediments (proximal): ~1.6 km³
Reconstructed Cone: ~2.4 km³
Deformed sediments: ~11 km³
Water depth
-2500 -2000 -1500 -1000 -500 m 0 500 1000
~10 km
B)
612 614 Easting (km) 620 622 624
no data
Deposit thickness
>500
400
300 m
200
100
0
Northing (km)
9396
9392
9388
C)
612 614 Easting (km) 620 622 624
no data
Erosion depth
120
90
60 m
30
0
Northing (km)
9396
9392
9388

A) Phase I: Deep-seated gradual spreading of the western flank of Ritter Island induces compressional deformation within the volcanic edifice and the neighboring seafloor sediments

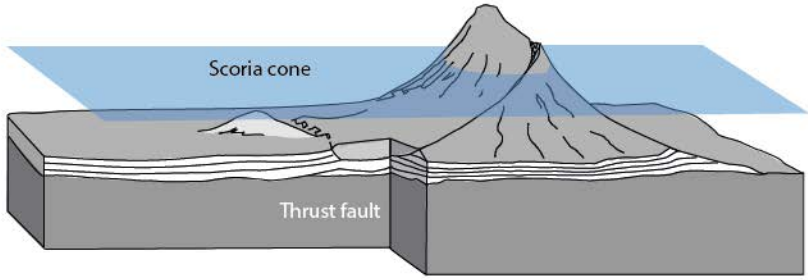

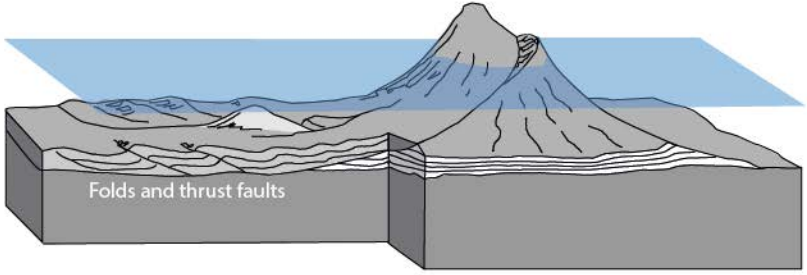

B) Phase I: Shearing within the western flank due to buttressing of the central flank segment by the pre-1888 scoria cone

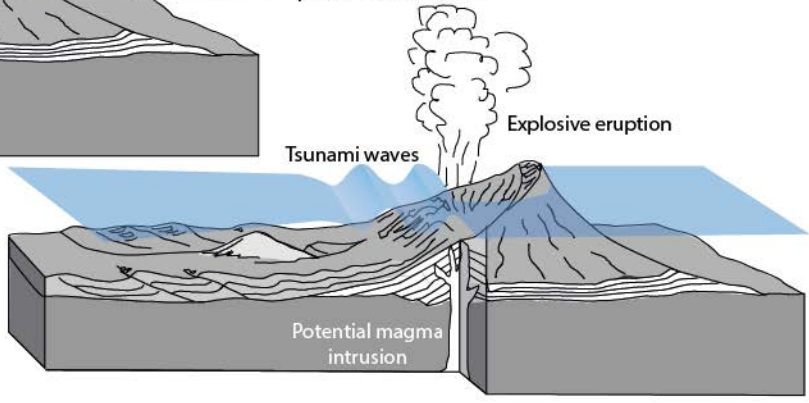

C) Phase II: Catastrophic collapse accompanied by an explosive eruption disintegrating the volcanic cone

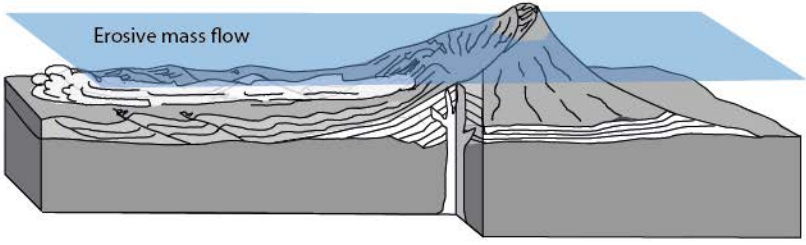

D) Phase II: Fast moving highly energetic mass flow erodes deeply into the previously deformed sediments and forms hummocky topography